A Novel Low-Temperature-Fired Multifunctional Varistor-Magnetic Ferrite Materials

Li-Then Mei, Hsing-I Hsiang, Hui-Wen Ye
National Cheng Kung University
No.1, University Road, National Cheng Kung University, Department of Resources Engineering
Tainan, Taiwan, R.O.C., 70101
Phone: 886-6-2757575-62821 E-Mail: n4895104@mail.ncku.edu.tw

Abstract

A novel low temperature-fired (950℃) multifunctional varistor-magnetic ferrite materials can be obtained by adding V_2O_5 into $CuCr_{0.2}Fe_{1.8}O_4$ ferrites. The relationship between the grain-boundary composition and varistor properties were investigated using scanning electron microscopy (SEM), transmission electron microscopy (TEM), energy dispersion spectroscopy (EDS), and X-ray photoelectric spectroscopy (XPS). The addition of V_2O_5 can effectively reduce the sintering temperature of $CuCr_{0.2}Fe_{1.8}O_4$ ferrites to temperatures of lower than 950℃. Moreover, the V^{5+} ions occupied the octahedral site of spinel structure and acted as donor dopant, which resulted in the semiconductive grain. The copper-rich observation at the grain boundary based on the TEM and EDS results implied that copper oxide would possibly develop at the grain boundary as the acceptor state, forming double Schottky barriers with the n-type semiconductor grains.

Key words: varistor, ferrite, low-temperature firing

I Introduction

The trends of the electronic devices are toward light and slim. The size of the final product can be reduced by integrating different kinds of passive components via cofiring technology [1-3]. Mismatched densification kinetics, chemical reaction and thermal expansion mismatch between the layers could generate undesirable defects such as delamination, cracks and camber in the final products [2-4]. To solve the densification and thermal expansion mismatch problems, a multi-functional material with simultaneously magnetic and varistor properties can be used to fabricate multi-functional passive devices.

ZnO varistors are widely used in electronic devices to protect devices from voltage surge. The varistor property originates from Schottky barrier [5] resulting from the n-type semiconductive grain and p-type or insulated grain-boundary [5-7]. In ZnO varistors, two kinds of additive oxides are used to improve varistor property [5,6]. One kind of cation dissolves in ZnO grains to increase the donor concentration, such as Co_2O_3, Mn_2O_3 [5,8]. The other one is an insoluble ion, which segregates at the grain-boundaries, so-called varistor former, such as BaO, Bi_2O_3, Pr_6O_{11} [5, 9]. In ZnO varistors, some varistor former can supply excess oxygen ions to the grain boundaries to form zinc vacancies and increase the acceptor concentration, such as Bi_2O_3 [6, 10]. The previous experimental data indicated that the trap density, donor concentration and barrier height for ZnO varistors, are about $10^{13}cm^{-2}$, $10^{17}cm^{-3}$ and ~0.8eV, respectively [5].

Spinel ferrites are commonly used as the raw materials of the magnetic components [11] to decrease the electromagnetic interference (EMI) of the electronic system [3]. Mayer [12] reported that the ferrites may exhibit varistor properties while Schottky barriers exist, which can be used to fabricate multifunctional varistor-magnetic devices. However, the multifunctional varistor-magnetic ferrites reported by Mayer was only speculative and no detailed formulation and process were described.

$CuCr_xFe_{2-x}O_4$ is a n-type conductor as x is equal to 0.2, [13]. $CuCr_2O_4$ can store or release oxygen at different temperature or atmosphere [14, 15]. V_2O_5 can act as a varistor former and sintering aid in ZnO varistor [16]. In this study, a novel low temperature-fired (950 ℃) multifunctional varistor-magnetic ferrite material was prepared by adding V_2O_5 into $CuCr_{0.2}Fe_{1.8}O_4$ ferrites. The relationship between the grain-boundary composition and varistor properties of V_2O_5 doped $CuCr_{0.2}Fe_{1.8}O_4$ ferrites were investigated using scanning electron microscopy (SEM), transmission electron microscopy (TEM), energy dispersion spectroscopy (EDS), and X-ray photoelectric spectroscopy (XPS).

II Experimental Procedures

$CuCr_{0.2}Fe_{1.8}O_4$ specimens were prepared using a conventional solid-state reaction and sintering process. The CuO (99.7%), Cr_2O_3 (98%), and Fe_2O_3 (99.9%) powders were mixed by ball milling with ZrO_2 balls for 12 hours. The mixed powders were calcined for 2 hours at 1000℃ in air after drying. X-ray diffraction identified a single spinel phase for the powders after calcinations. V_2O_5 (99.5%) powders were added into the calcined powders with a composition expression, such as (100-x) mol% $CuCr_{0.2}Fe_{1.8}O_4$ + x mol% V_2O_5 (x = 0.5, 1, 2), abbreviate as CCFO05, CCFO1, CCFO2. These mixed powders were milled again for 24 hours. After milling, 1wt% polyvinyl alcohol (PVA) was added into the powders to help the formation of compacts. The powders were then uniaxially pressed at 100MPa into disks of 8mm in diameter and 2mm in thickness. The greens were sintered at 900℃~1000℃ at an interval of 50℃ in air for 2 hours, cooled to 500℃ at 2℃/min then furnace cooled to room temperature.

The bulk density was calculated through the dry weight, diameter and thickness of the sample. The crystalline phase identification was determined using X-ray diffractometry (Siemens, D5000) with Cu-Kα radiation. In-Ga electrodes were rubbed on the sample surface for electrical conduction analyses. The specimen I-V curves were measured using a Keithley 2410 source meter. Then the electrical field versus current density diagram was obtained through the geometry factor of the sample. Complex impedance were measured at 1V over the frequency range from 20Hz to 1MHz using a precision LCR meter (HP 4284A). The impedance contribution from grain can be separated from impedance spectrum [17,18]. After measuring the impedance spectra at different temperature, we can obtain the activation energy for the grain through the Arrhenius equation. The Arrhenius equation is described as $\sigma = \sigma_0 \exp\left(\frac{-E_a}{kT}\right)$, where σ, σ_0, E_a, k are the conductivity, pre-exponential factor, activation energy, Boltzmann constant, respectively.

Field emission scanning electron microscopy (FE-SEM, JEOL JSM-6700F) was employed to observe the specimen microstructure and grain size.

Before SEM observation, the specimens were polished and thermal etched at 850℃ for 30 minutes. A field emission transmission electron microscope (FEI, Tecnai G2 F20) equipped with a high-angle annular dark field (HAADF) detector was used for Z-contrast (Z: atomic number) images. Energy dispersive spectroscopy (EDS) was used to compare the grain and grain-boundary compositions. CCFO1 sintered at 900 ℃ was chose for FE-TEM observation.

A CCFO2 specimen sintered at 900℃ was polished using SiC abrasive paper to obtain a polished surface. Another CCFO2 specimen sintered at 900℃ was rapped using a hammer to obtain a fracture surface. The polished (PS) and fracture specimens (FS) were cleaned in acetone. The FS grain boundaries remained on the surface because of the relatively weak linkage between grains. X-ray photoelectron spectroscopy (XPS) (ESCA PHI 1600, Physical Electronics) measurement was performed on both PS and FS with Mg Kα (1253.5eV) radiation. The sample charge produced by irradiation was determined by measuring the shift in the C 1s signal given by a binding energy of 284.5eV. The X-ray photoelectron spectra were simulated using XPSPEAK41.

The M-H curve was measured using a superconducting quantum interference device magnetometer (MPMS SQUID VSM, Quantum Design) to obtain the coercive force and remanent flux density.

III Results and Discussion

Figure 1 shows the X-ray diffraction patterns of the powders after calcination and the sample after sintering. There was no distinct difference between the powders after calcination and the sample after sintering. The theoretical density calculated from the XRD result of the powders after calcination is 5.389g/cm^3. The bulk density for the specimens added with various amount of V_2O_5 sintering at different temperatures is shown in Fig.2. The sample added with 0.5mol% V_2O_5, CCFO0005, cannot be densified at 900℃. The bulk density increased with increasing sintering temperature for CCFO1 specimens. The bulk density decreased with increasing sintering temperature for CCFO2 specimens, which may be due to the over-sintering.

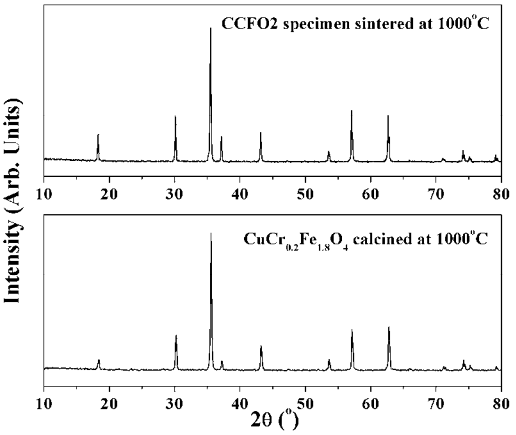

Fig. 1 X-ray diffraction patterns of the powders after calcination and the sample after sintering.

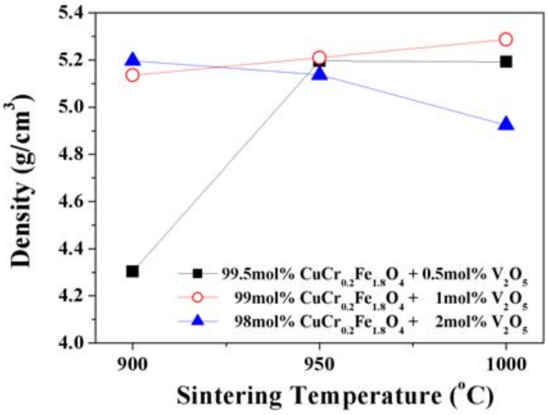

Fig. 2 Bulk density for the specimens added with various amount of V_2O_5 sintering at different temperatures.

Figure 3 shows the SEM images of the CCFO05 and CCFO2 specimens sintered at various temperatures. Figure 4 shows the average grain size for the specimens, indicating that the average grain size increased with increasing sintering temperature. Discontinuous grain growth was found in Figs. 3(b) and 3 (d).

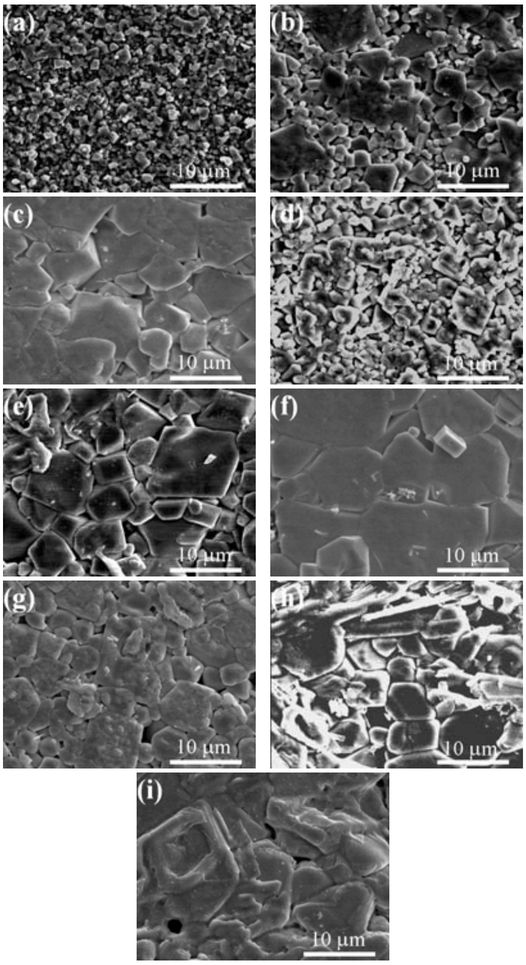

Fig. 3 SEM images for CCFO05 specimens sintered at (a) 900℃, (b) 950℃, (c) 1000℃; CCFO1 specimens sintered at (d) 900℃, (e) 950℃, (f) 1000℃; CCFO2 specimens sintered at (g) 900 ℃, (h) 950℃, (i) 1000℃

Figure 5 shows the high-angle annular dark field (HAADF) image for CCFO1 sintered at 900℃. The compositions at different places shown in Fig. 5 are listed in table I. In the HAADF-STEM imaging, the image intensity is approximately proportional to the square of the atomic number termed as Z-contrast imaging and atomic column occupancy, allowing heavy atoms to be visualized directly from the image contrast features.

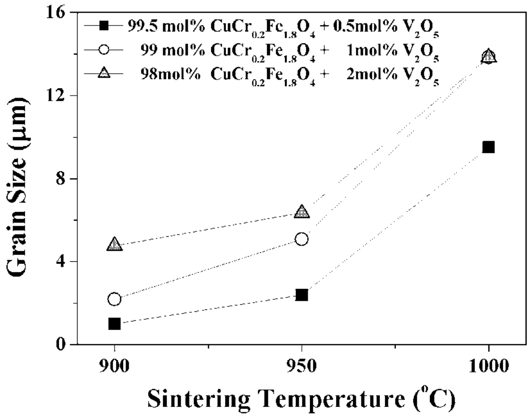

Fig.4 Average grain size of the CCFO05 and CCFO2 specimens sintered at various temperatures.

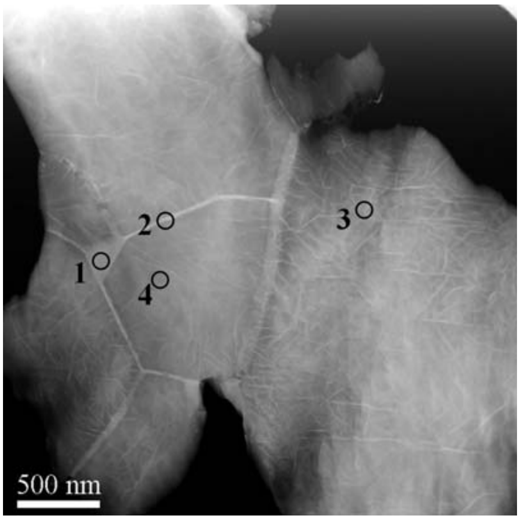

Fig. 5 High-angle annular dark field (HAADF) image for CCFO1 specimen sintered at 900℃.

Table I Energy dispersive spectroscopy (EDS) analyses results for Fig. 5.

Atom% Position	Cu	Fe	Cr	V
1	96.93	2.26	0.47	0.34
2	92.70	6.10	0.92	0.28
3	58.73	37.55	3.59	0.14
4	2.03	90.00	7.89	0.09

Thus the bright region in Fig.5 can be attributed to Cu-rich phase due to copper has the largest atomic number in CCFO1 specimens. Table I and Fig. 5 show that copper-rich phase may segregate at grain-boundaries and triple junctions, and precipitate in the interiors of the grains. This copper-rich phase(s) may increase the acceptor concentration at the grain-boundaries and enhance the varistor property [19]. The diffraction pattern at position 3 in Fig. 5 is shown in Fig. 6. Figure 7 shows the diffraction pattern after treating with logarithmic calculation of Fig. 6. Cu-Cr spinel phase will decompose to $CuCrO_2$, Cr_2O_3, or CuO at high temperature [15]. The copper-poor region occurred at position 4 in Fig. 5 may due to the decomposition for Cu-Cr ferrite. Table I also reveal that the grains contain a small amount of vanadium.

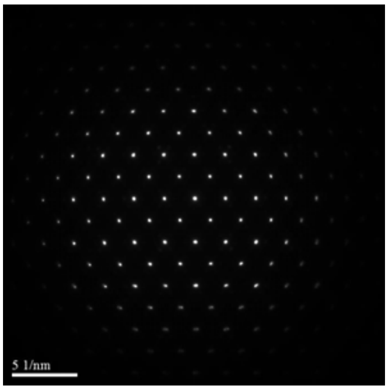

Figure 6 Diffraction pattern at position 3 in Fig. 5.

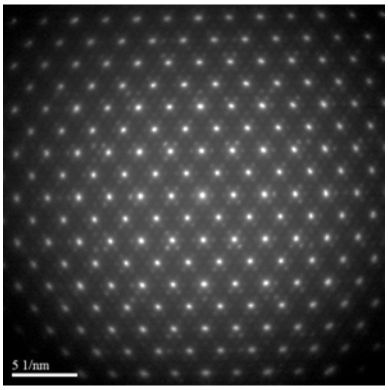

Fig. 7 Diffraction pattern after treating with logarithmic calculation of Fig. 6.

The copper XPS results for FS and PS samples are shown in Figs. 8 and 9, respectively. The simulation results indicate that the peak at between 928eV to 938eV can be deconvoluted into two peaks for the FS and PS samples. These two peaks can be assigned to Cu^{+} and Cu^{2+} [20]. The total Cu^{2+} $2p_{3/2}$ peak area is larger than the Cu^{+} $2p_{3/2}$ peak in FS. Conversely, the Cu^{+} $2p_{3/2}$ peak area is larger than the Cu^{2+} $2p_{3/2}$ peaks in PS. These results suggest that FS sample contained more Cu^{2+} than PS, which may be due to the grain-boundaries exhibit higher oxygen partial pressure than grains. The XPS results show that the valence of chromium and vanadium are 3 and 5, respectively.

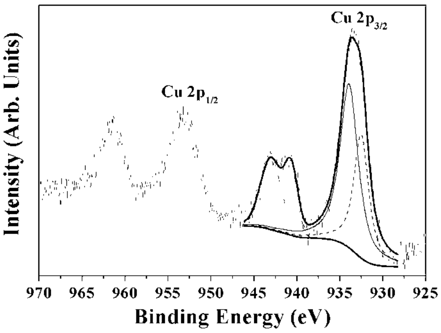

Fig. 8 X-ray photoelectric spectroscopy (XPS) spectrum of Cu 2p for the fracture surface of CCFO2 sintered at 900 ℃ . The dash line represents Cu^{+} $2p_{3/2}$ peak.

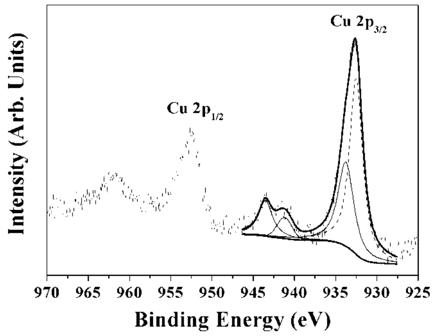

Fig. 9 X-ray photoelectric spectroscopy (XPS) spectrum of Cu 2p for the polished surface of CCFO2 sintered at 900 ℃ . The dash line represents Cu^{+} $2p_{3/2}$ peak.

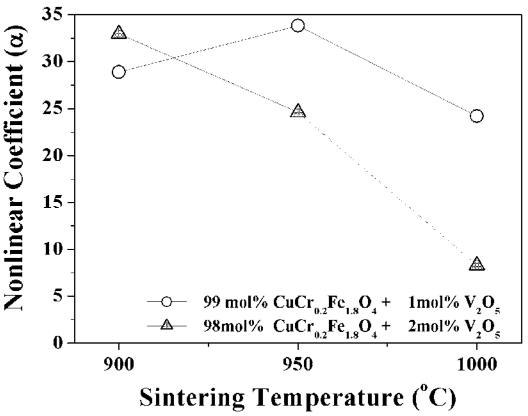

Fig. 10 Non-linear coefficient for the specimens under different processing conditions.

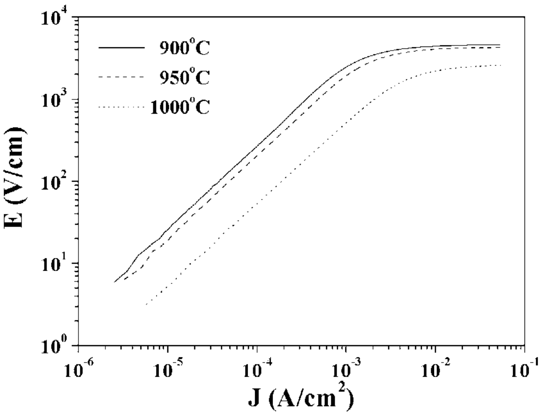

Fig. 11 J-E curve for CCFO2 specimens under different sintering temperature.

The non-linear coefficient (α, 10^{-2}~$10^{-1.5}$A/cm^2) for the specimens is shown in Fig.10. The non-linear coefficient of CCFO05 specimens are not shown in Fig.10, because the specimens were breakdown during the I-V curve measurement. CCFO05 specimen after sintering at 1000 ℃ exhibited non-ohmic property and the non-linear coefficient was about 35 at the first I-V curve measurement. However, it was breakdown after the second measurement. The non-linear coefficient for CCFO1 specimen sintered at 950℃ is larger than the specimen sintered at 900℃, which may be due to the grain growth. After grain growth, the microstructure and grain size distribution were more uniform. While an electric field was applied on a specimen with nonuniform microstructure and broad grain size distribution, such as CCFO1 specimen sintered at 900℃, the path of the current would not go through the high resistance Schottky barriers, but concentrate at the region with low resistance, which led to the non-linear coefficient decreased. The non-linear coefficient for CCFO1 specimen sintered at 950℃ was larger than the specimen sintered at 1000℃, which may due to the grain size effect. For CCFO2 specimens, the non-linear coefficient decreased with increasing sintering temperature due to the same reason. The number of grain-boundary per unit volume is proportion to grain size. When the grain size increased, the I-V curve would shift downward and rightward due to the lower electric field applied on the grain-boundaries. The current density (J) versus electric field (E) curves for the CCFO2 specimens sintered at different temperatures are shown in Fig. 11. The J-E curve was shifted downward and rightward as the sintering temperature was raised due to the increase of the grain size of CCFO2 with increasing sintering temperature. According to the definition of the non-linear coefficient, the displacement of the J-E curve, caused part of the ohmic region was included to the calculation for non-linear coefficient. Therefore the non-linear coefficient decreased with increasing temperature for CCFO2 specimens.

Figure 12 shows the complex impedance plane plots for the CCFO1 specimen sintered at 900℃. The left and right part for the semi-circle in Fig.12 is not symmetry, suggesting that there are two semi-circles [18, 21] in Fig.12. The left part of the semi-circle represents the grain impedance, and the right part of the semi-circle represents the grain boundary impedance. The activation energies for the specimens are shown in Fig. 13. The activation energy for CCFO05 specimen was about 0.5eV and CCFO1 and CCFO2 were both about 0.37eV. The activation energy for CCFO05 specimen sintered at 900℃ is not shown in Fig.13, because the specimen is not dense enough. According to the TEM and activation energy results, vanadium would dissolve into the grain and act as donor dopant to increase the conductivity of the grain.

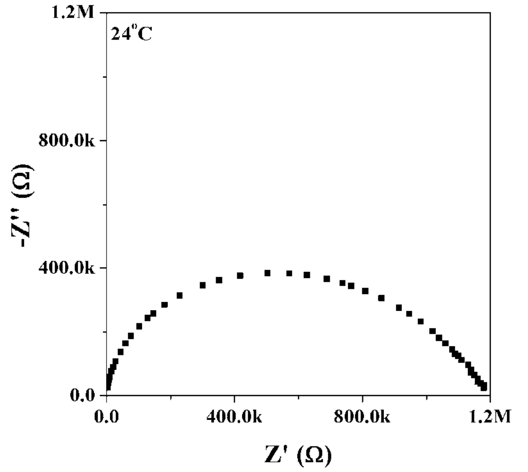

Fig. 12 Complex impedance plane plots at room temperature for CCFO1 specimen sintered at 900 ℃.

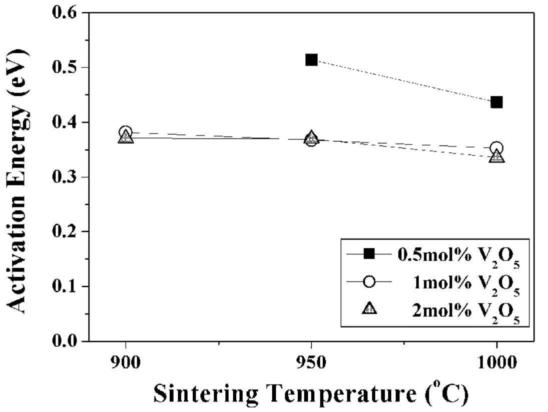

Fig. 13 Activation energies for the specimens added with 0.5-2 mol% V_2O_5 sintered at different temperatures.

The M-H curve for CCFO1 specimen sintered at 900℃ is shown in Fig. 14. The coercive force and remanent flux density are 200Oe and 9.848emu/g, respectively. These results suggest that CCFO specimens are soft magnetic materials.

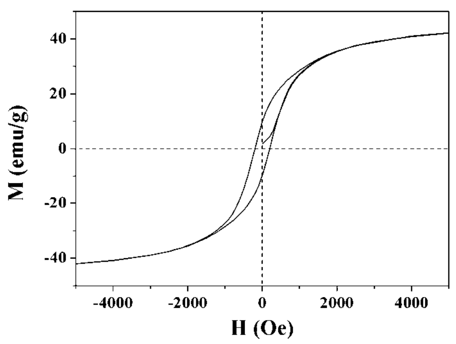

Fig. 14 M-H curve for CCFO1 specimen sintered at 900℃.

IV Conclusion

The addition of V_2O_5 can effectively reduce the sintering temperature of $CuCr_{0.2}Fe_{1.8}O_4$ ferrites to temperatures of lower than 950℃. Moreover, the V^{5+} ions occupied the octahedral site of spinel structure and acted as donor dopant, which resulted in the semiconductive grain. The segregation of copper rich phase(s) at the grain-boundary may increase the acceptor concentration, and hence improve the varistor property. The $CuCr_{0.2}Fe_{1.8}O_4$ ferrite added with 1-2 mol%V_2O_5 sintered at 900℃ exhibited both magnetic and varistor properties, which can be a good candidate material for the application in ESD and EMI.

Reference

[1] John Rector, Joseph Dougherty, Vernon Brown, John Galvagni, John Prymak, “Integrated and Integral Passive Components: A Technology Roadmap”, Proceedings of the 1997 Electronic Components and Technology Conference (ECTC), San Jose, CA, USA, May 18-21, pp. 713-723, 1997.

[2] Balasubramaniam Vaidhyanathan, Ketharam Annapoorani, Jon Binner, “Microwave Sintering of Multilayer Integrated Passive Devices”, Journal of the American Ceramic Society, Vol. 93, No. 8, pp. 2274-2280, February, 2010.

[3] A. Rafferty, Y. Gun’ko, R. Raghvendra, “An Investigation of Co-Fired Varistor-NiZn Ferrite Multilayers”, Materials Research Bulletin, Vol. 44, No. 4, pp. 747-752, April, 2009.

[4] Jui-Chu Jao, Pang Li, Sea-Fue Wang, “Characterization of Inductor with Ni-Zn-Cu Ferrite Embedded in B_2O_3-SiO_2 Glass”, Japanese Journal of Applied Physics, Vol. 46, No. 9A, pp.5792-5796, September, 2007.

[5] David R. Clarke, “Varistor Ceramics”, Journal of the American Ceramic Society, Vol. 82, No. 3, pp.485-502, February, 1999.

[6] Tapan K. Gupta, “Application of Zinc Oxide Varistors”, Journal of the American Ceramic Society, Vol. 73, No. 7, pp.1817-1840, April, 1990.

[7] Michio Matsuoka, Takeshi Masuyama, Yoshio Iida, “Voltage Nonlinearity of Zinc Oxide Ceramics Doped with Alkali Earth Metal Oxide”, Japanese Journal of Applied Physics, Vol. 8, pp.1275-1276, August, 1969.

[8] Naoki Ohashi, Yoshihiro Terada, Takeshi Ohgaki, Shigeru Tanaka, Takaaki Tsurumi, Osamu Fukunaga, Hajime Haneda, Junzo Tanaka, ”Synthesis of ZnO Bicrystal Doped with Co or Mn and Their Electrical Properties”, Japanese Journal of Applied Physics, Vol. 38, No. 9A, pp.5028-5032, June, 1999.

[9] Aldo B. Alles, Vernon L. Burdick, “The Effect of Liquid-Phase Sintering on the Properties of Pr_6O_{11}-Based ZnO Varistors”, Journal of Applied Physics, Vol. 70, No. 11, pp.6883-6890, December, 1991.

[10] F. Stucki, F. Greuter, “Key Role of Oxygen at Zinc Oxide Varistor Grain Boundaries”, Applied Physics Letters, Vol. 57, No. 5, pp. 446-448, July, 1990.

[11] Mitsuo Sugimoto, “The Past, Present, and Future of Ferrites”, Journal of the American Ceramic Society, Vol. 82, No. 2, pp.269-280, January, 1999.

[12] Ferdy Mayer, “Non-Linear Conduction and Low-Pass Effects: Their Combined Use in New System Oriented EMC-Suppression Techniques”, Proceedings of the 1993 Electromagnetic Compatibility, IEEE International Symposium, Dallas, Texas, August 9-13, pp. 348-351, 1993.

[13] C. Venkateshwarlu, D. Ravinder, “High Temperature Thermoelectric Power Studies of Cu-Cr Ferrites,” Journal of Alloys and Compounds, Vol. 397, No. 1-2, pp. 5-8, March, 2005.

[14] K. S. De, J. Ghose, K. S. R. C. Murthy, “Electrical Properties of the $CuCr_2O_4$ Spinel Catalyst,” Journal of Solid State Chemistry, **43** [3] 261-266 (1982)

[15] James D. Stroupe, “An X-Ray Diffraction Study of Copper Chromites and of the ‘Copper-Chromium Oxide’ Catalyst”, Journal of the American Chemistry Society, Vol. 71, No. 2, pp. 569-572, February, 1949.

[16] Jyh-Kuang Tsai, Tai-Bor Wu, “Microstructure and nonohmic properties of binary ZnO-V_2O_5 ceramics sintered at 900℃”, Materials Letters, Vol. 26, No. 3, pp. 199-203, February, 1996.

[17] D. C. Sinclair, A. R. West, “Impedance and Modulus Spectroscopy of Semiconducting

$BaTiO_3$ Showing Positive Temperature Coefficient of Resistance", Journal of Applied Physics, Vol. 66, No. 8, pp.3850-3856, October, 1989.

[18] D. Arcos, M. Vázquez, R. Valenzuela, M. Vallet-Regí, "Grain boundary impedance of doped Mn-Zn ferrites", Journal of Materials Research, Vol. 14, No. 3, pp.861-865, March, 1999.

[19] Li-Then Mei, Hsing-I Hsiang, Tsang-Tse Fang, "Effect of Copper-Rich Secondary Phase at the Grain Boundaries on the Varistor Properties of $CaCu_3Ti_4O_{12}$ Ceramics", Journal of the American Ceramic Society, Vol. 91, No. 11, pp. 3735-3737, November, 2008.

[20] N. S. Mclntyre, M. G. Cook, "X-ray Photoelectron Studies on Some Oxides and Hydroxides of Cobalt, Nickel, and Copper", Analytical Chemistry, Vol. 47, No. 13, pp. 2208-2213, 1975.

[21] John T. S. Irvine, Derek C. Sinclair, Anthony R. West, "Electroceramics: Characterization by Impedance Spectroscopy", Advanced Materials, Vol. 2, No. 3, pp. 132-138, March 1990.